Supplementary Information

A Novel Strategy for Discovering Inorganic Solar-Cell Absorbers: Leveraging Octahedral Features in ABX_3 Structure

Wonzee Jung[1,2], Suim Lim[1,3], Yong Youn[1], Jiho Lee[4], Awet Mana Amare[5], Shah Syed Fawad[5], Inyoung Jeong[5], Donghyeop Shin[5], Joo Hyung Park[5], Kihwan Kim[5], and Kanghoon Yim[1*]

[1*]Energy AI and Computational Science Laboratory, Korea Institute of Energy Research, Daejeon, 34129, Korea.

[2]Department of Physics, Chungnam National University, Daejeon, 34134, Korea.

[3]Department of Mechanical Engineering, Sogang University, Seoul, 04107, Korea.

[4]Department of Materials Science and Engineering, Seoul National University, Seoul, 08826 , Korea.

[5]Photovoltaics Research Department, Korea Institute of Energy Research, Daejeon, 34129, Korea.

[*]E-mails: kyjung1020@kier.re.kr, khyim@kier.re.kr

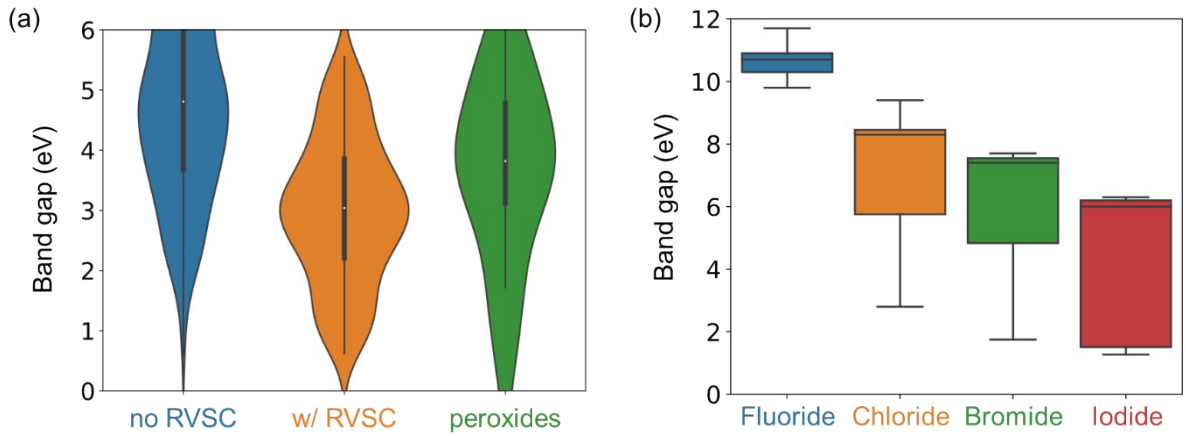

Figure S1. (a) The violin plot for calculated band gap distribution of binary and ternary oxides from ref. [1]. (b) The box plot of experimental band gap distribution for fluorides, chlorides, bromides, and iodides from ref. [2-8].

(a)

⓪ Corner 100%

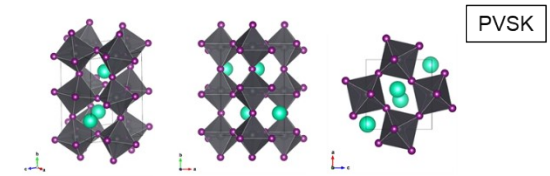

A	B	Dimension
Not octa	Corner 100%	3D

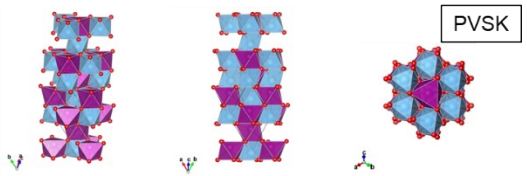

A	B	Dimension
Corner 100%	Corner 100%	3D

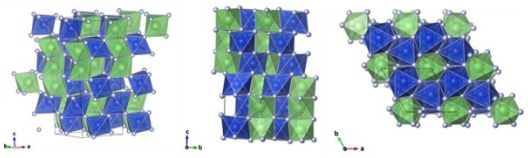

A	B	Dimension
Face 100%	Corner 100%	1D-3D hybrid

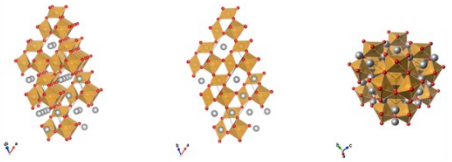

A	B	Dimension
Not octa	Corner 100%	3D

(b)

① Corner + Edge

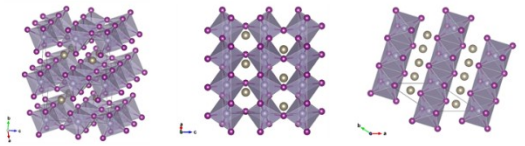

A	B	Dimension
Not octa	Corner 33% Edge 67%	2D-like

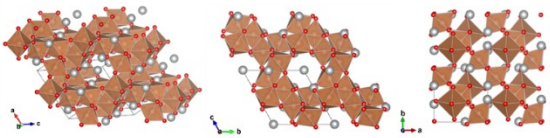

A	B	Dimension
Not octa	Corner 67% Edge 33%	3D

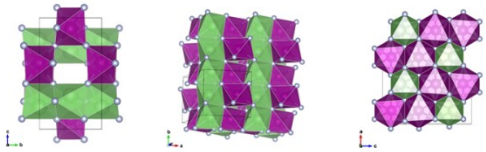

A	B	Dimension
Face 100%	Corner 33% Edge 67%	1D-3D hybrid

(c)

② Corner + Face

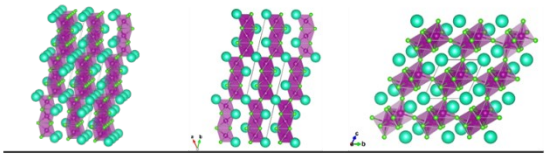

A	B	Dimension
Not octa	Corner 33% Face 67%	3D

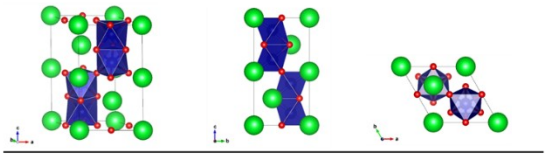

A	B	Dimension
Not octa	Corner 50% Face 50%	3D

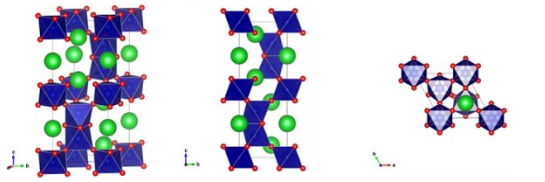

A	B	Dimension
Not octa	Corner 67% Face 33%	3D

(d)

③ Edge 100%

SL

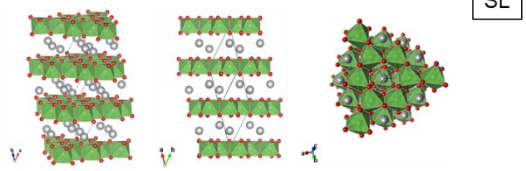

A	B	Dimension
Not octa	Edge 100%	2D-like

SW

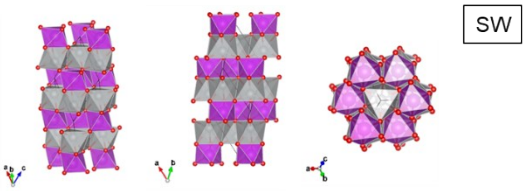

A	B	Dimension
Edge 100%	Edge 100%	2D-like

DL2D

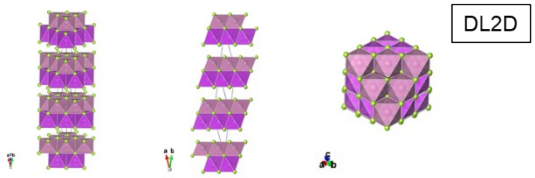

A	B	Dimension
Edge 100%	Edge 100%	2D

δ+2D

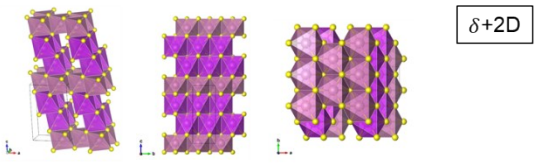

A	B	Dimension
Edge 67% None 33%	Edge 100%	1D-2D hybrid

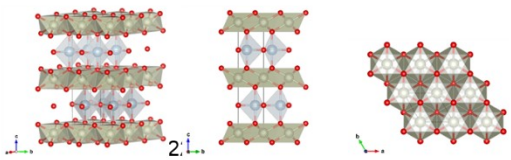

A	B	Dimension
Not octa	Edge 100%	2D-like

(e)

④ Edge + none

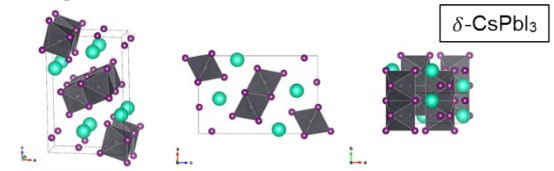

A	B	Dimension
Not octa	Edge 67% None 33%	1D-like

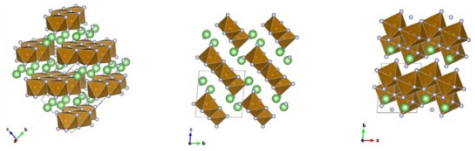

A	B	Dimension
Not octa	Edge 67% None 33%	1D-like

(f)

⑤ Face 100%

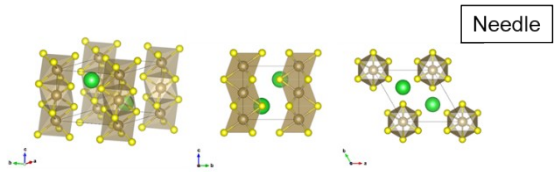

A	B	Dimension
Not octa	Face 100%	1D-like

Figure S2. Representative types of structures based on octahedral interconnections and dimension. The structures consist of (a) only corner sharing, (b) corner and edge sharing, (c) corner and face sharing, (d) only edge sharing, (e) edge and none sharing, and (f) only face sharing are shown

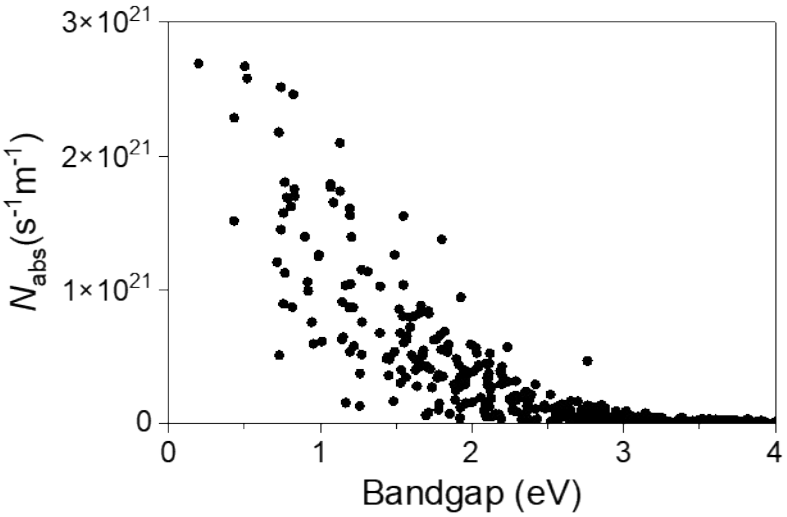

Figure S3. Relation of light absorption to band gaps

Table S1. Decomposition energies of chalcogenide materials to competitive phases.

Material	Competitive phases		Decomposition E (meV/atom)	
	Formula	ICSD ids	GGA	SCAN
$SbBiSe_3$	$\frac{1}{2}Bi_2Se_3+\frac{1}{2}Sb_2Se_3$	617072, 651516	-19	-266
$InSbSe_3$	$\frac{1}{2}In_2Se_3+\frac{1}{2}Sb_2Se_3$	4478, 651516	**+37**	**+33**
$SbYTe_3$	$\frac{1}{2}Y_2Te_3+\frac{1}{2}Sb_2Te_3$	653174, 185952	-25	-40
$InBiSe_3$	$\frac{1}{2}In_2Se_3+\frac{1}{2}Bi_2Se_3$	4478, 617072	**+2**	**+11**
$LaSbSe_3$	$\frac{1}{10}La_{10}Se_{19}+\frac{11}{30}Sb_2Se_3+\frac{4}{15}Sb$	69730, 651516, 651489	-19	-122
$BiInS_3$	$\frac{1}{2}In_2S_3+\frac{1}{2}Bi_2S_3$	151644, 30775	**+2**	-10

(c) $CsSnI_3$ (mp-616378)

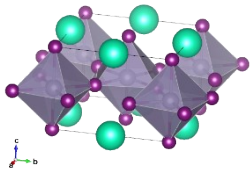

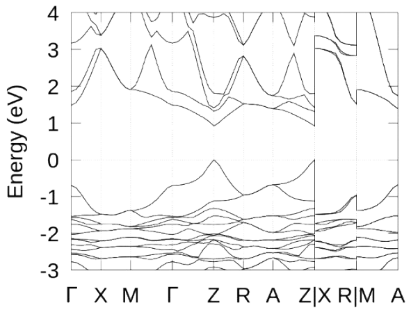

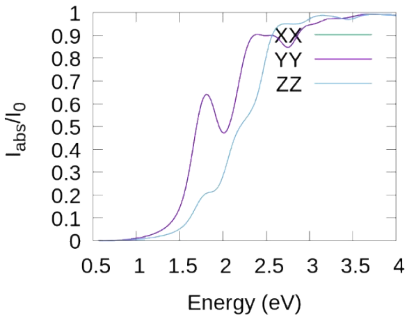

(d) $CsPbI_3$ (mp-1069538)

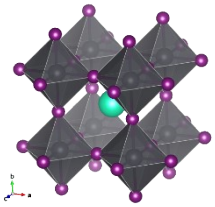

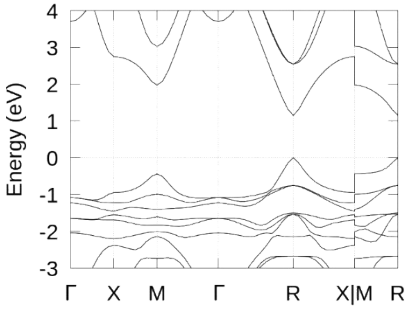

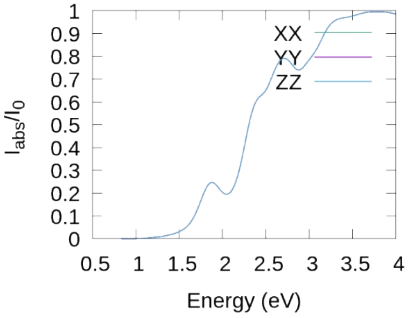

(a) $RbGeI_3$ (mp-571458)

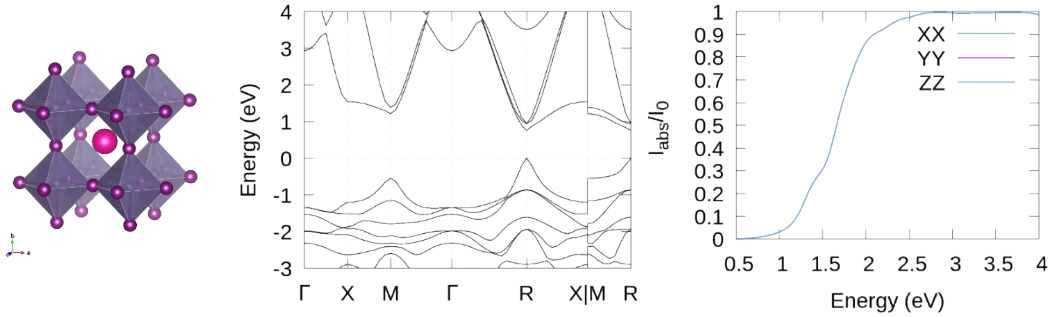

(b) $CsSnI_3$ (mp-568570)

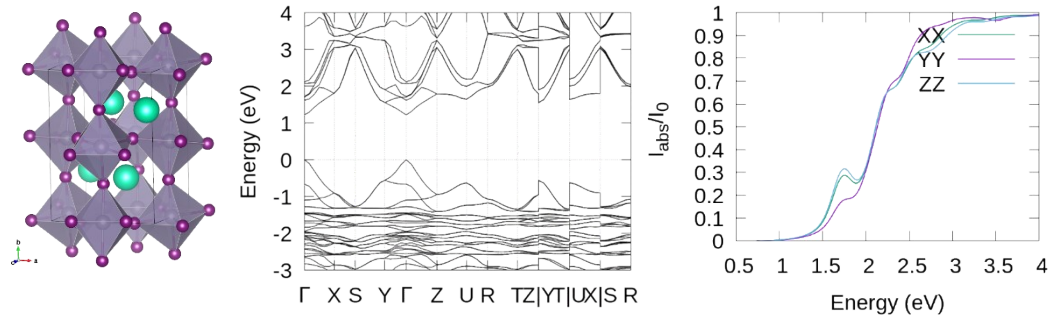

(e) $CsSnBr_3$ (mp-27214)

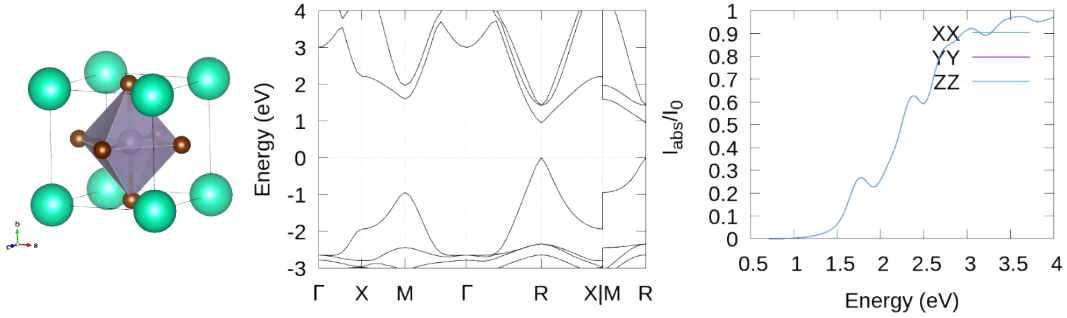

(f) $CsGeI_3$ (mp-28377)

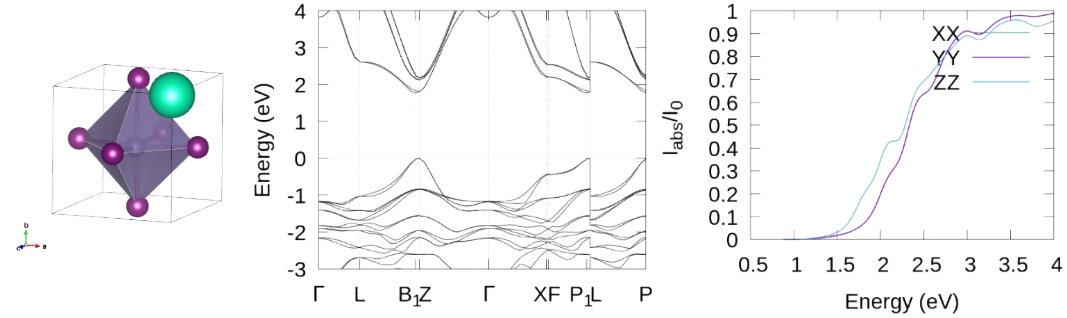

(g) $RbSnBr_3$ (mp-998157)

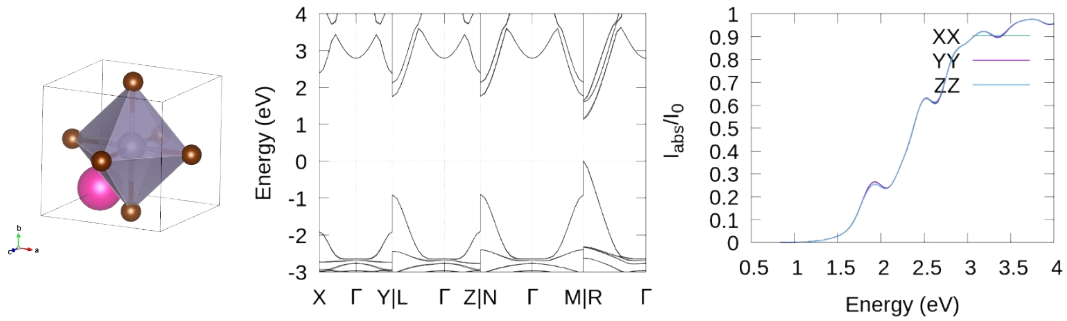

(h) $CsSnI_3$ (mp-614013)

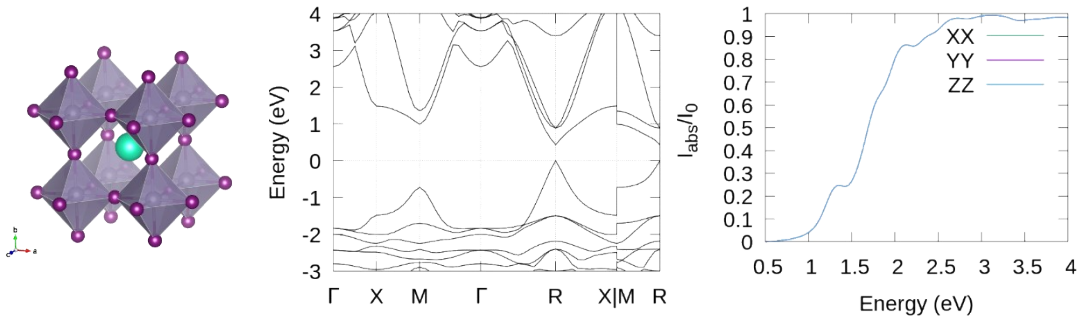

(i) $CsGeI_3$ (mp-642690)

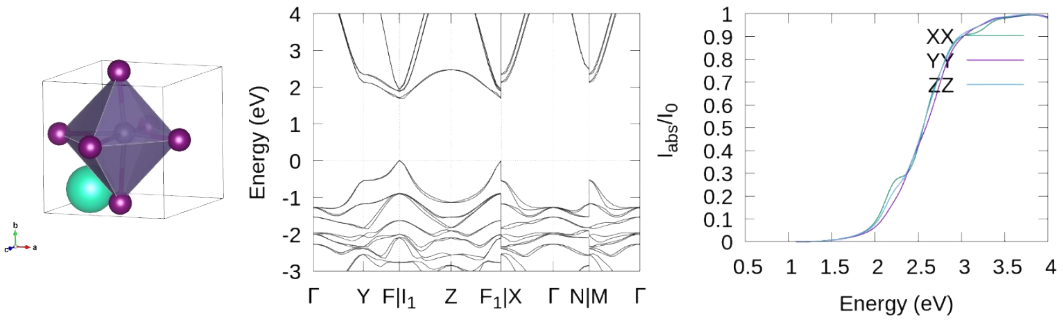

(j) $LaSbSe_3$ (mp-1222966)

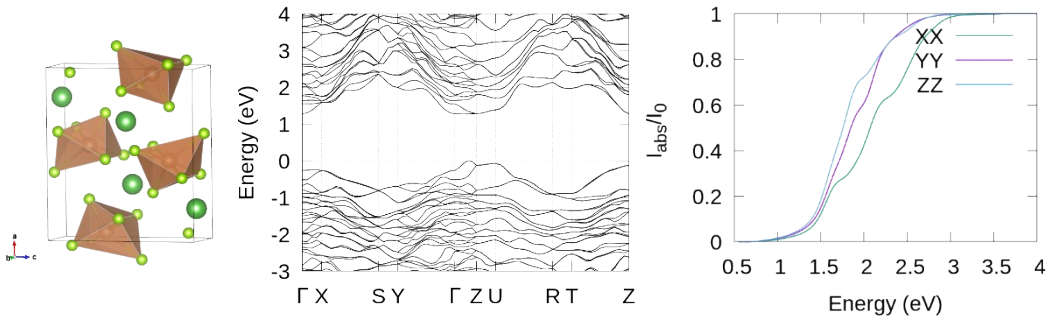

(k) $BiInS_3$ (mp-1078776)

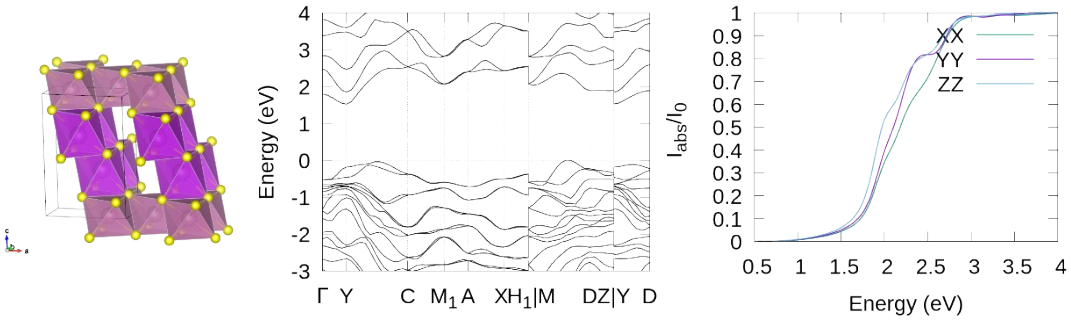

(l) $SrZrS_3$ (mp-5193)

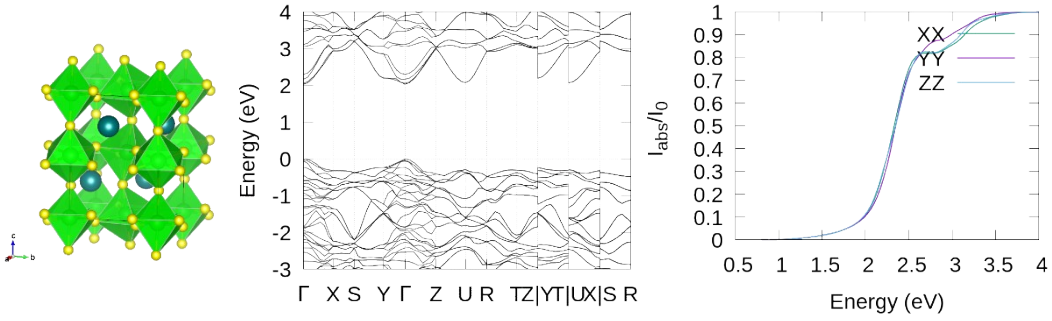

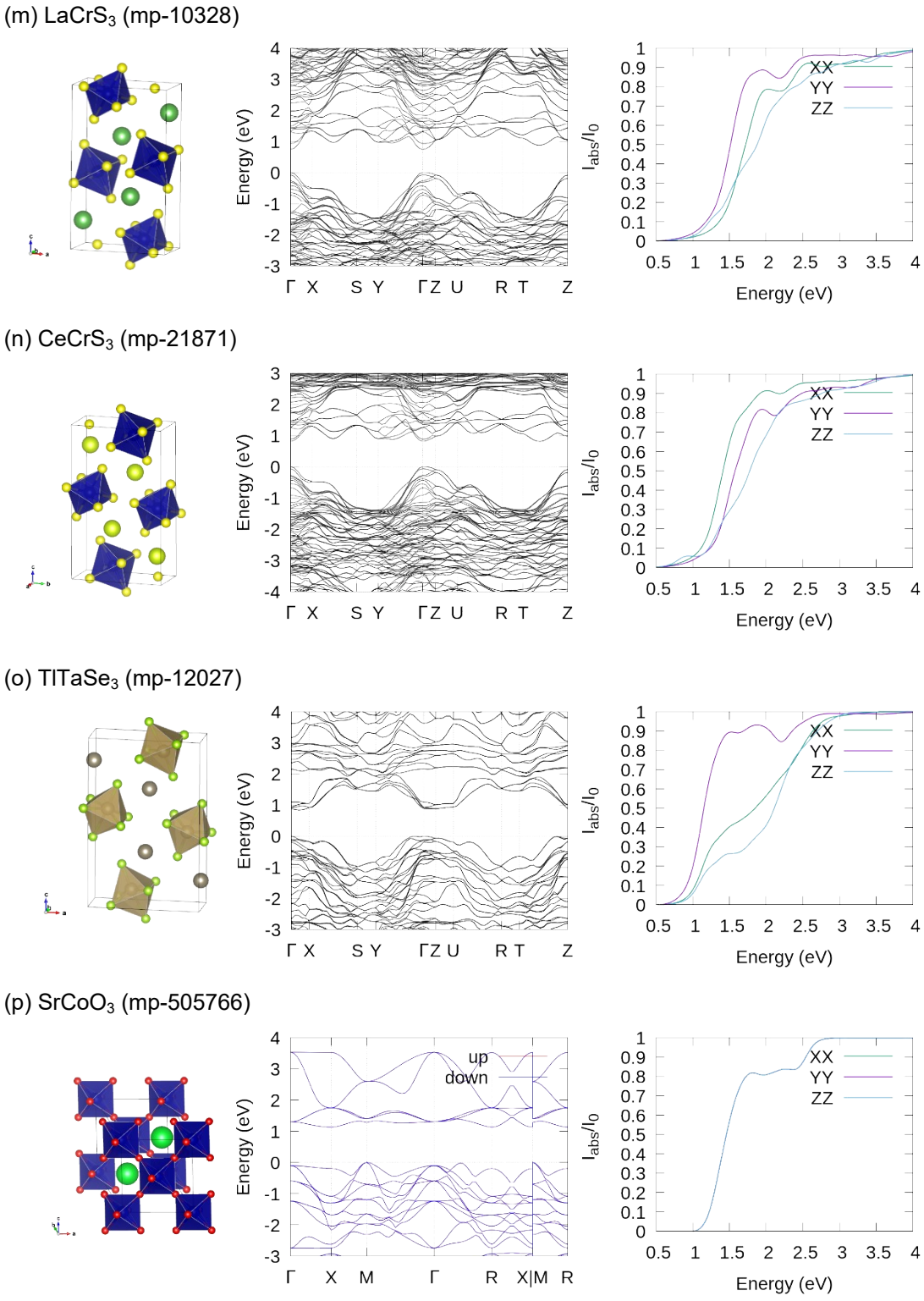

Figure S4. DFT results for unit-cell structure, band structures, and absorptivities of top 20 candidate materials with highest figure of merit (FoM); (a) $RbGeI_3$ (mp-571458), (b) $CsSnI_3$ (mp-568570), (c) $CsSnI_3$ (mp-616378), (d) $CsPbI_3$ (mp-1069538), (e) $CsSnBr_3$ (mp-27214), (f) $CsGeI_3$ (mp-28377), (g) $RbSnBr_3$ (mp-998157), (h) $CsSnI_3$ (mp-614013), (i) $CsGeI_3$ (mp-642690), (j) $LaSbSe_3$ (mp-1222966), (k) $BiInS_3$ (mp-1078776), (l) $SrZrS_3$ (mp-5193), (m) $LaCrS_3$ (mp-10328), (n) $CeCrS_3$ (mp-21871), (o) $TlTaSe_3$ (mp-12027), and (p) $SrCoO_3$ (mp-505766).

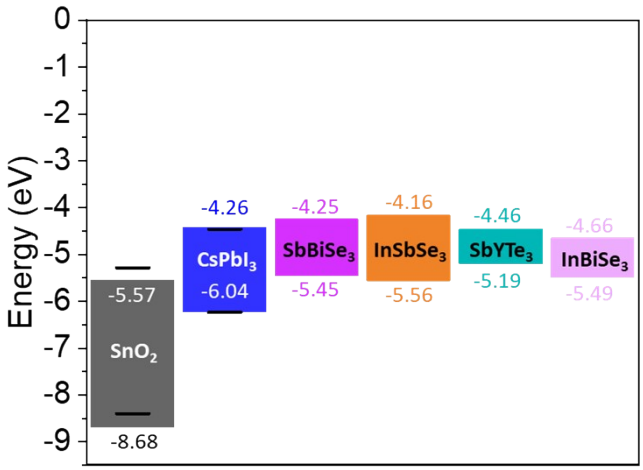

Figure S5. Band edge positions of SnO_2, $CsPbI_3$, $SbBiSe_3$, $InSbSe_3$, $SbYTe_3$, and $InBiSe_3$. Following the methodology of previous study[9], the bandgap centers relative to the vacuum level were calculated at the GGA level. The VBM and CBM positions were then corrected using experimental band gaps(SnO_2[10] and $CsPbI_3$[11]) or HSE06 band gaps($SbBiSe_3$, $InSbSe_3$, $SbYTe_3$, and $InBiSe_3$). The black lines are experimental band edge positions in previous literatures[10,11].

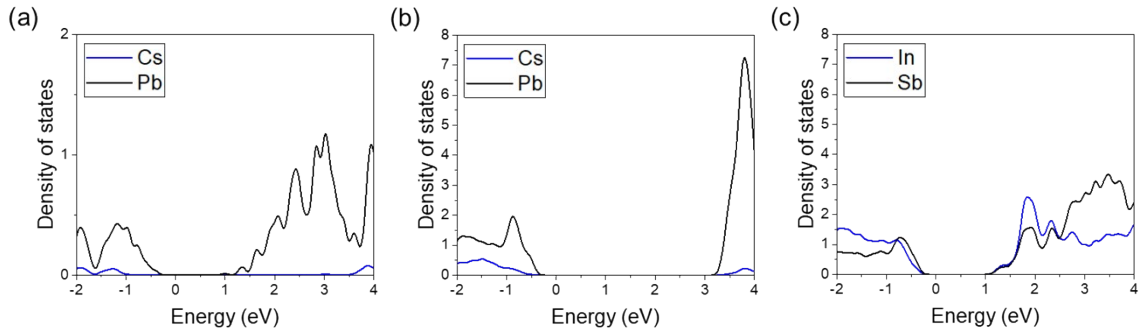

Figure S6. Projected density of states (PDOS) of cations for (a) α-$CsPbI_3$, (b) δ-$CsPbI_3$, and (c) $InSbSe_3$. The PDOS calculations were performed using the GGA functional, with band gap corrections using the HSE06 functional.

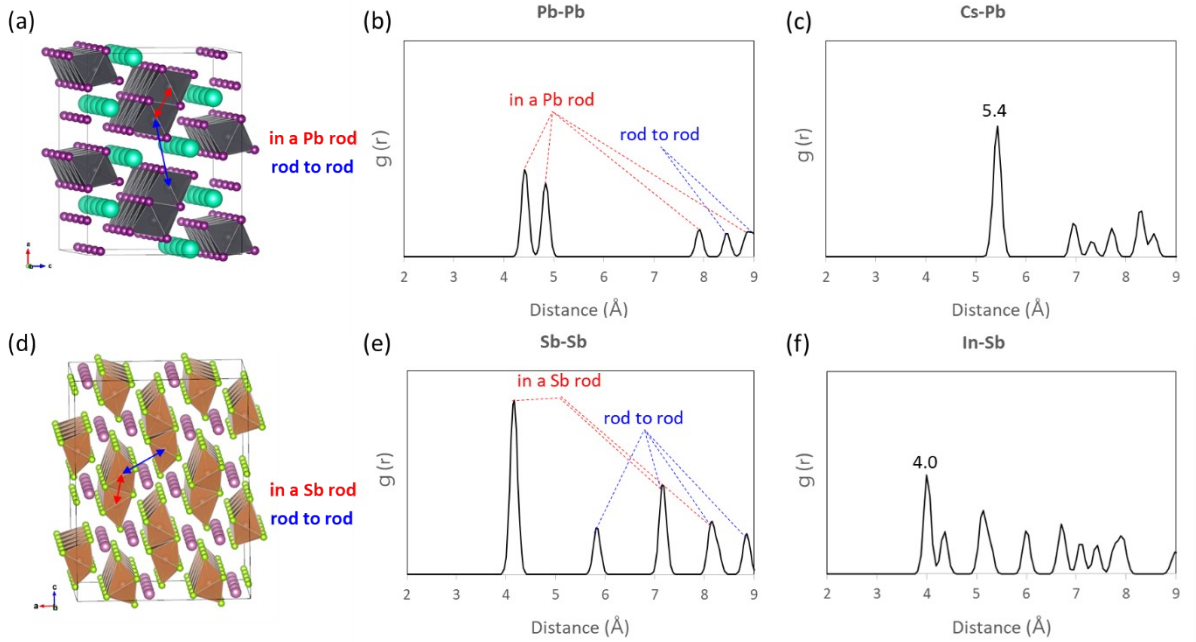

Figure S7. Partial pair distribution functions (PDFs) for (a) Pb-Pb and (b) Cs-Pb in $\delta-$ $CsPbI_3$, and (c) Sb-Sb and (d) In-Sb in $InSbSe_3$.

To further clarify the underlying reasons behind the differing trends in terms of octahedral interconnections between halides and chalcogenides, we have conducted a detailed comparisons between two representative materials, $CsPbI_3$ and $InSbSe_3$. This study aimed to understand why $InSbSe_3$, which has a similar octahedral structure to δ-$CsPbI_3$, exhibits promising photovoltaic properties, while $CsPbI_3$ loses its excellent characteristics through a phase transition from the α to δ phase.

First, projected density of state (PDOS) of α-$CsPbI_3$, δ-$CsPbI_3$, and $InSbSe_3$ (Fig. S6) reveals that Cs shows no contribution to the band-edge states in both α-, and δ-$CsPbI_3$. In contrast, both In and Sb in $InSbSe_3$ significantly contribute to the band-edge states. Due to the 1D-like octahedral interconnections of PbI_3 in δ-$CsPbI_3$, the A-site cations (Cs) act as barriers to charge transport between the PbI_3 octahedral rods. Whereas, in $InSbSe_3$, both In and Sb function as transport paths for each other, facilitated by their joint contribution to the band edge states.

Secondly, we focused on the structural differences between δ-$CsPbI_3$ and $InSbSe_3$. Despite the similarity in their octahedral interconnections, which contain BX_3 1D rods, the two structures are precisely distinct. The partial pair distribution functions (PDFs) indicate that closest Sb-Sb distances between two adjacent $SbSe_3$ rods in $InSbSe_3$ are much closer than Pb-Pb distances across PbI_3 rods in δ-$CsPbI_3$ (~ 5.9 Å vs. ~ 8.4 Å, see Fig. S7(b,e)) Refer to the Cs-Pb and In-Sb PDFs in each materials (as shown in Fig. S7(c,f)), we could infer these differences primarily arise from the relative sizes of the A cations (Cs vs. In).

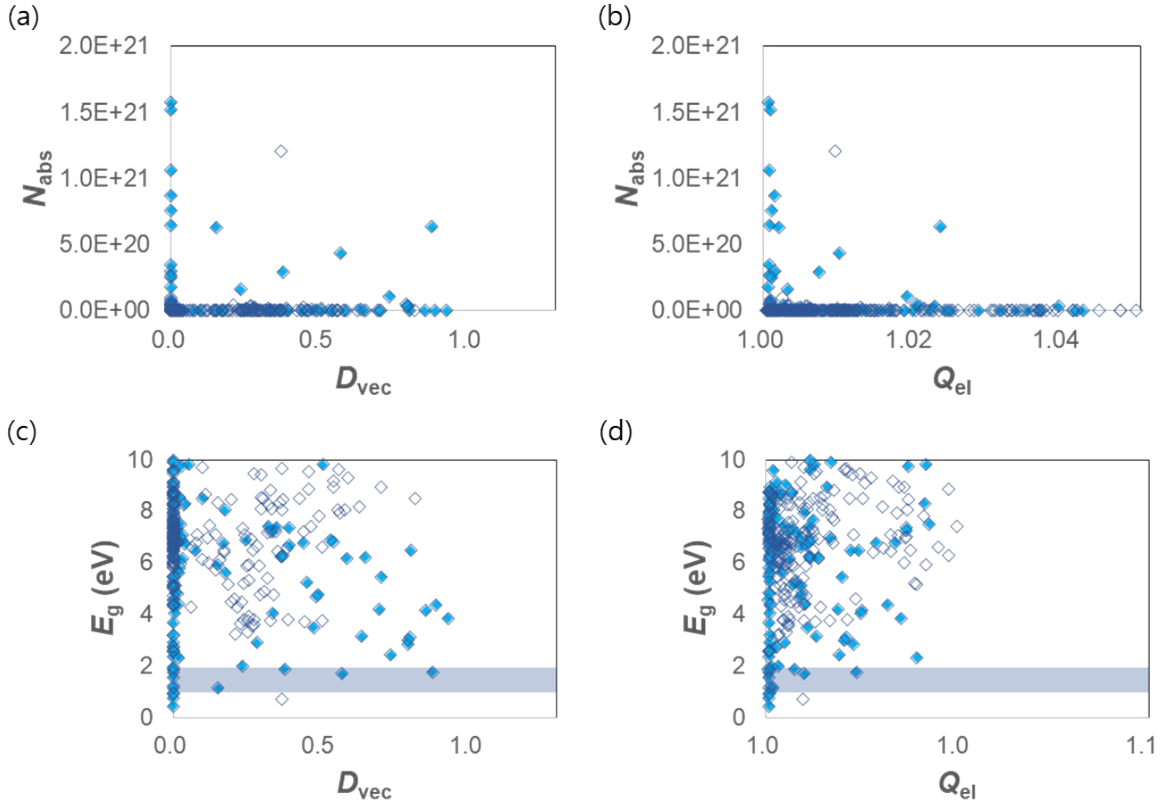

Figure S8. Distribution of light absorptions in total halides (unfilled symbol) and fully corner-sharing halides (filled symbol) according to the (a) distortion vector index (D_{vec}), and (b) quadratic elongation (Q_{el}). Distribution of band gap in the same materials according to (c) D_{vec}, and (d) Q_{el}.

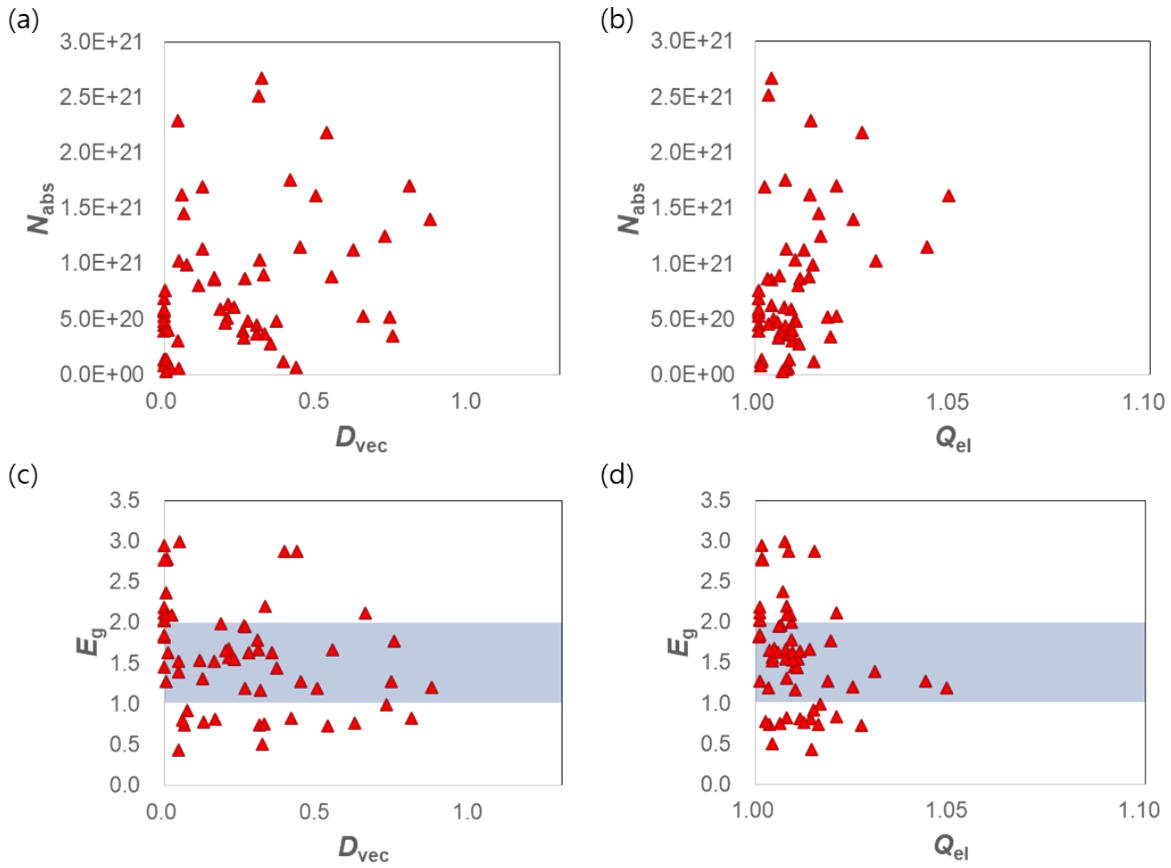

Figure S9. Distribution of light absorptions in chalcogenides according to the (a) distortion vector index (D_{vec}), and (b) quadratic elongation (Q_{el}). Distribution of band gap in the same materials according to (c) D_{vec}, and (d) Q_{el}.

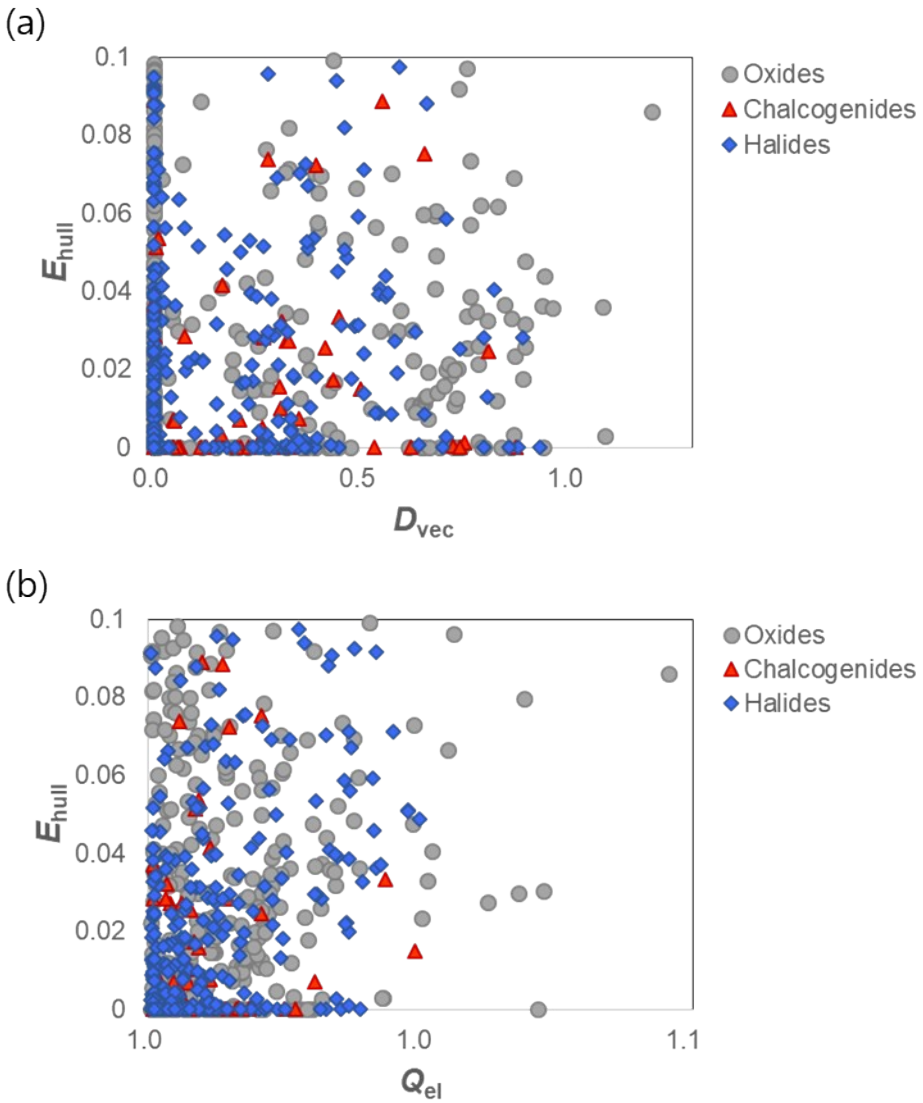

Figure S10. Energy above hull distribution according to (a) distortion vector index (D_{vec}), and (b) quadratic elongation (Q_{el}).

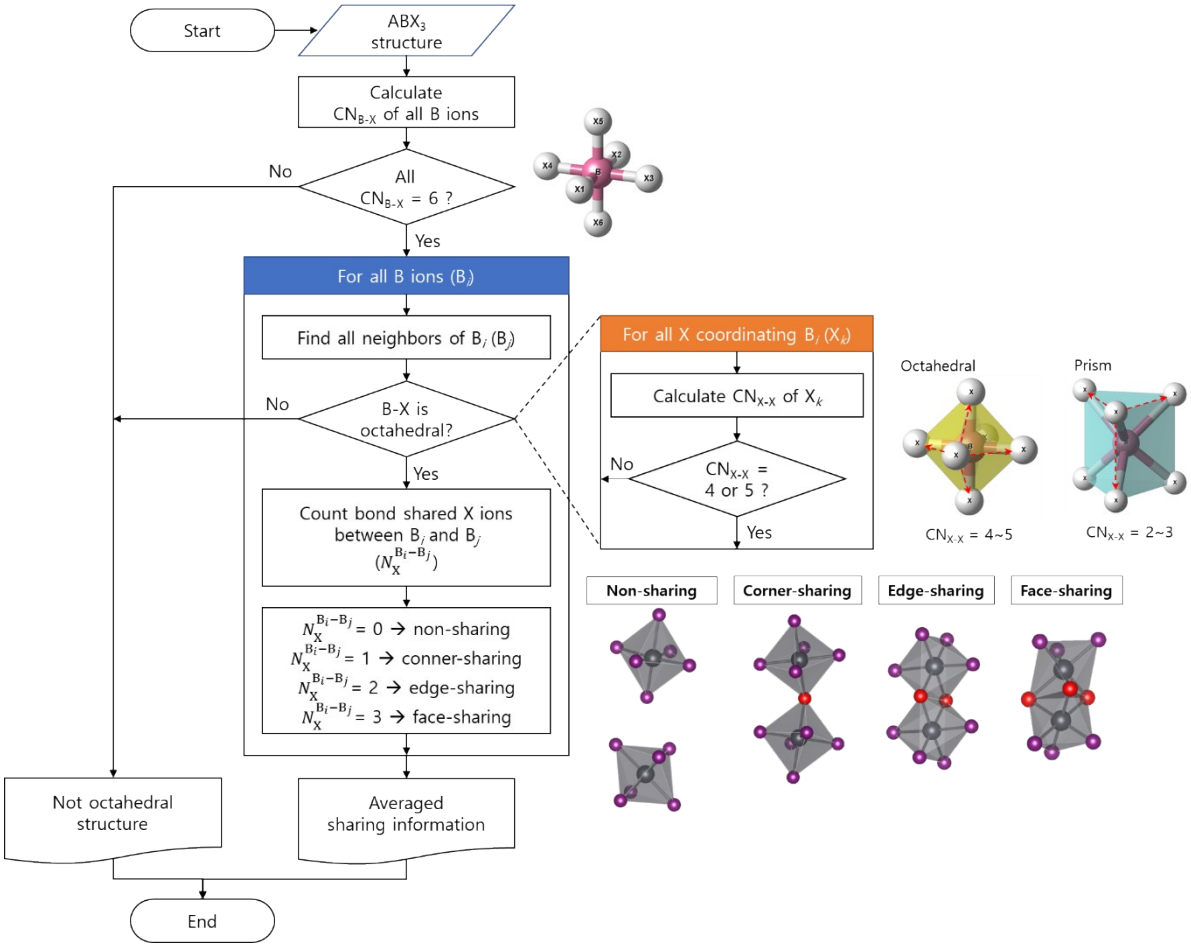

Figure S11. The Flowchart of our in-house code for detecting octahedral structures and classifying their interconnections.

(a)

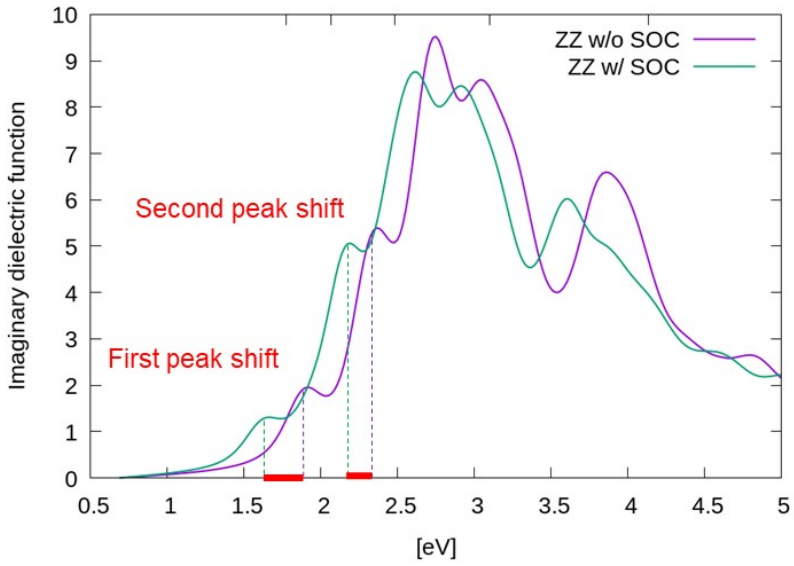

(b)

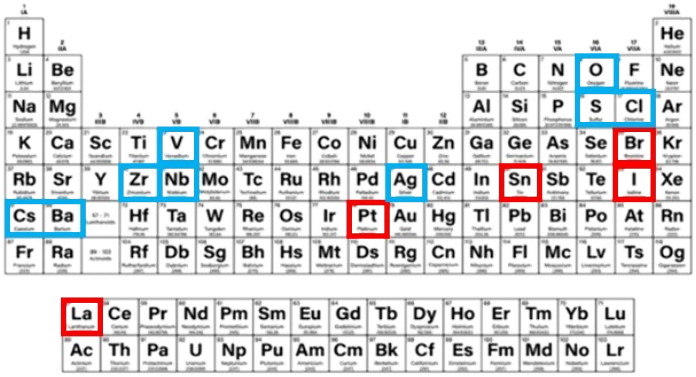

Materials	First peak shift (eV)	Second peak shift (eV)
$BaZrS_3$	0.00	0.00
$CsVCl_3$	+0.01	+0.01
$AgNbO_3$	-0.09	+0.03
$CsCaBr_3$	-0.14	-0.10
$CsSnCl_3$	-0.33	-0.28
$CsCaI_3$	-0.22	-0.16
$LaFeO_3$	+0.14	-0.15
$BaPtO_3$	-0.00	+0.27

Figure S12. (a) Example of peak shift in the imaginary part of the dielectric function with SOC consideration. The violet line represents result without SOC consideration, while the green line represents result with SOC consideration. (b) Tested elements, and the peak shift in the imaginary part of the dielectric function in the ZZ direction with SOC consideration.
Reproduced by Wonzee, J., (2022). *First-principles study of perovskite solar cells for long-term stability* [Unpublished master's thesis]. Chungnam National Univ.

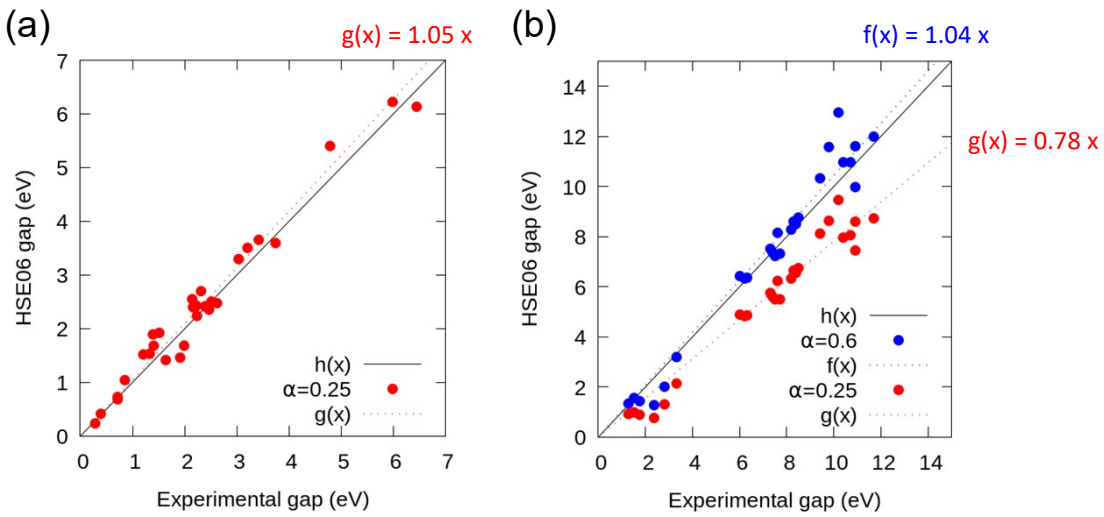

Figure S13. Comparison between theoretical and experimental band gaps[2-8] for (a) compounds with group IV, V, and VI anions, and (b) halides. In halides, the hybrid mixing ratio $\alpha = 0.6$ gives more accurate prediction for experimental band gaps.
Reproduced by Wonzee, J., (2022). *First-principles study of perovskite solar cells for long-term stability* [Unpublished master's thesis]. Chungnam National Univ.

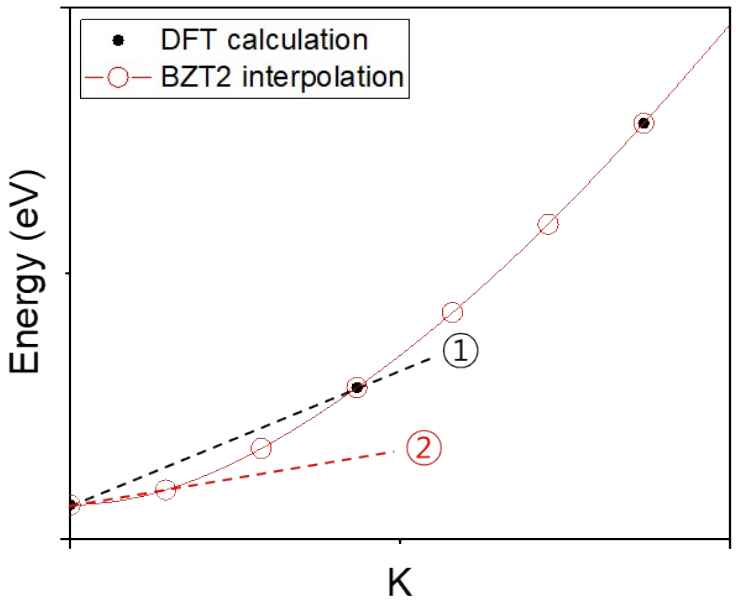

Figure S14. Schematic E-K diagram comparing DFT calculation results and their BZT2 interpolation results. ① represents an extension connecting the first and second points of the DFT results, while ② represents extension of BZT2 interpolation results.

Appendix. Practical mean of electron and hole effective masses

Given that ionized defect scattering is dominant in crystalline semiconductors, the relationship between the conductivity σ and effective mass m^* is approximately as follows[12,13]:

$$\sigma \propto \frac{1}{\sqrt{m^*}} \quad \text{(Eq. S1)}$$

Since the conductivity σ is a function of electron mobility μ_e, and hole mobility μ_h and they are also inversely proportional to $\sqrt{m^*}$ as below,

$$\sigma = en\mu_e + ep\mu_h \quad \text{(Eq. S2)}$$

$$\mu \propto \frac{1}{\sqrt{m^*}} \quad \text{(Eq. S3)}$$

practical mean of electron and hole effective mass can be defined as follows:

$$\mu_{mean} \equiv \frac{\mu_e + \mu_h}{2} \propto \frac{\frac{1}{\sqrt{m^*_e}} + \frac{1}{\sqrt{m^*_h}}}{2} \quad \text{(Eq. S4)}$$

$$m^*_{mean} \equiv \left(\frac{2\sqrt{m^*_e m^*_h}}{\sqrt{m^*_e} + \sqrt{m^*_h}} \right)^2 \quad \text{(Eq. S5)}$$

Considering the Eq. S1, the practical mean of effective masses m^*_{mean} is applied to FoM in inversed square root form.

References

[1] K. Yim, Y. Yong, J. Lee, K. Lee, H.-H. Nahm, J. Yoo, C. Lee, C. Seong Hwang and S. Han, *NPG Asia Mater*., 2015, **7**, e190–e190.

[2] J. Heyd, J. E. Peralta, G. E. Scuseria and R. L. Martin, *J. Chem. Phys.*, 2005, **123**, 174101.

[3] J. Paier, R. Asahi, A. Nagoya and G. Kresse, *Phys. Rev. B***,** 2009**, 79**, 115126.

[4] C. R. Gopikrishnan, D. Jose and A. Datta, *AIP Adv.*, 2012, **2**, 012131.

[5] L.-y. Huang and W. R. L. Lambrecht, *Phys. Rev. B*, 2013, **88**, 165203.

[6] A. N. Belsky, P. Chevallier, E. N. Mel'chakov, C. Pédrini, P. A. Rodnyi and A. N. Vasil'ev, *Chem. Phys. Lett.*, 1997**, 278**, 369–372.

[7] S. Ono, R. El Ouenzerfi, A. Quema, H. Murakami, N. Sarukura, T. Nishimatsu, N. Terakubo, H. Mizuseki, Y. Kawazoe and A. Yoshikawa, *Jpn. J. Appl. Phys.*, 2005, **44**, 7285.

[8] C. C. Stoumpos, L. Frazer, D. J. Clark, Y. S. Kim, S. H. Rhim, A. J. Freeman, J. B. Ketterson, J. I. Jang and M. G. Kanatzidis, *J. Am. Chem. Soc.*, 2015, **137**, 6804–6819.

[9] M. C. Toroker, D. K. Kanan, N. Alidoust, L. Y. Isseroff, P. Liao and E. A. Carter, *Phys. Chem. Chem. Phys.*, 2011, **13**, 16644–16654.

[10] H. Hosono, *Recent Progress in Transparent Electronics*, Wiley, 2010, chapter 2.

[11] S. Tao, I. Schmidt, G. Brocks, J. Jiang, I. Tranca, K. Meerholz and S. Olthof, *Nat. Commun.*, 2019**, 10**, 2560.

[12] J. M. Ball and A. Petrozza, *Nat. Energy*, 2016, **1**, 11.

[13] E. Conwell and V. F. Weisskopf, *Phys. Rev.*, 1950, **77**, 388–390.